Chemie Ingenieur Technik

Improved Preparation of Cu/Zn-Based Catalysts by Well-Defined Conditions of Co-Precipitation and Aging

David Guse[1,*], Sabrina Polierer[2], Stefan Wild[2], Stephan Pitter[2], and Matthias Kind[1,*]

DOI: 10.1002/cite.202100197

Supporting Information available online

Dedicated to Prof. Dr. Thomas Hirth on the occasion of his 60th birthday

In order to enable science- and knowledge-based adaptation of catalyst materials to new demands, e.g., methanol synthesis from CO_2, a modified method to prepare Cu/Zn-based catalysts based on the strict consecutive execution of co-precipitation and aging is investigated. By successfully stabilizing the initial co-precipitate, two mixing regimes are revealed: regarding slow mixing, the particle size of the co-precipitate decreases with increasing volume flow. By contrast, co-precipitation is no longer influenced by mixing for sufficiently high volume flows. While aging can be accelerated by forming smaller aggregates in the co-precipitation, the final state is found to be defined by thermodynamic equilibrium alone. Furthermore, the microstructure of the final catalyst was influenced and the performance in direct dimethyl ether synthesis was improved by adjusting the mixing in the co-precipitation. We believe that the approach could be scaled-up to industrial production rates and, hence, is promising to make methanol synthesis from CO_2 more effective and sustainable.

Keywords: Catalyst preparation, Continuous co-precipitation, Copper-zinc catalyst, Mixing, Particle formation

Received: November 04, 2021; *revised:* January 13, 2022; *accepted:* January 20, 2022

1 Introduction

Methanol (MeOH), with a worldwide production capacity of 83 million tons in 2019 [1], is a key commodity in the chemical industry [2]. In addition, applications in the mobility sector using MeOH as a raw material for synthetic fuel components, such as dimethyl ether (DME), are of growing importance [3, 4]. Nowadays, MeOH is produced mainly from syngas, according to Eqs. (1) and (2), using Cu/ZnO-based catalysts [5]. DME can be consecutively produced by MeOH dehydration, according to Eq. (3), using an additional acid dehydration catalyst.

$$CO + 2\ H_2 \rightleftharpoons CH_3OH\ (MeOH) \quad (1)$$

$$CO_2 + 3\ H_2 \rightleftharpoons CH_3OH + H_2O \quad (2)$$

$$2\ CH_3OH \rightarrow H_2O + CH_3OCH_3\ (DME) \quad (3)$$

Up to now, syngas has been produced primarily by coal gasification or natural gas reforming, resulting in a syngas rich in CO and H_2. Continued development of catalysts over many years has led to $Cu/ZnO/Al_2O_3$ (CZA) being the preferred composition of industrial catalysts for this syngas [6]. However, there is an increased need currently for the development of process routes to MeOH and DME that use syngas from sustainable sources. In addition to green H_2 generated from electrolysis by solar or wind power, increased use of CO_2 from the atmosphere or industrial waste streams requires modified catalysts and suitable catalyst preparation technologies [6, 7].

High MeOH productivity [8] and selectivity [9] are generally target qualities for catalyst development. These qualities correlate with the high mass-specific surface area of Cu,

[1]David Guse, Prof. Dr.-Ing. Matthias Kind
david.guse@kit.edu, matthias.kind@kit.edu
Karlsruhe Institute of Technology (KIT), Institute of Thermal Process Engineering (TVT), Kaiserstraße 12, 76131 Karlsruhe, Germany.

[2]Sabrina Polierer, Stefan Wild, Dr. Stephan Pitter
Karlsruhe Institute of Technology (KIT), Institute of Catalysis Research and Technology (IKFT), Hermann-von-Helmholtz-Platz 1, 76344 Eggenstein-Leopoldshafen, Germany.

which forms the catalytically active sites, and a homogeneous and periodic distribution of Cu and ZnO [8, 10, 11]. The ZnO prevents the sintering of individual Cu crystallites and enhances the MeOH selectivity due to chemically bound interfaces of Cu and ZnO [10, 12]. A fine dispersion of the promoter Al_2O_3 further improves the activity and stability [13, 14]. However, if water is present, according to Eq. (2), ZrO_2 seems to be a more favorable promoter [6, 15]. Therefore, Cu/ZnO/ZrO_2 (CZZ) is considered in the context of our studies.

One approach to obtain the homogeneous distribution of Cu and ZnO on the nanoscale in the final catalyst is to achieve the preferential formation of the crystalline phase zincian malachite ($Cu_{(2-x)}Zn_xCO_3(OH)_2$) in a catalyst precursor. Here, up to 31 at % Zn are periodically incorporated inside a Cu-based crystal lattice [16]. During calcination, zincian malachite subsequently decomposes into CuO and ZnO, according to Eq. (4), while preserving the arrangement of Cu and Zn atoms defined by the crystal lattice of zincian malachite, as illustrated in Fig. 1. This results in the desired homogeneous nanostructure of the final catalyst [17]. However, zincian malachite, also named rosasite, is not formed directly from the reactants but through a complex transition of intermediates during the aging step.

$$Cu_{(2-x)}Zn_xCO_3(OH)_2 \rightarrow (2-x)\ CuO + x\ ZnO + CO_2 + H_2O \quad (4)$$

This opens the idea of a multistep preparation. Firstly, a co-precipitate as homogeneous as possible is formed by co-precipitation from dissolved Cu and Zn salts and an alkaline solution. Initial co-precipitate particles are usually firmly intergrown aggregates of single-phase primary particles, e.g., $Cu(OH)_2$, $Zn(OH)_2$ [18] and georgeite ($Cu_2CO_3(OH)_2$) [19], see Fig. 1. These aggregates typically agglomerate and age. That makes it difficult to characterize their particle properties in the initial state. On the one hand, studies by Jiang et al. [20, 21] showed that different mixing geometries in the co-precipitation affect the homogeneity of Cu/Zn distribution in the co-precipitate and, subsequently, the microstructure of the final catalyst. Furthermore, Zhang et al. [22] determined improvements in the physicochemical properties of CZA catalyst precursors and the subsequent catalyst performance for a continuous co-precipitation compared to a semi-batch process. On the other hand, Simson et al. [23] found no significant differences in precatalysts prepared by batch co-precipitation in a stirred tank reactor and the continuous operating mode in a micromixer, respectively. Similarly, simulations and experimental studies by Hartig et al. [24] indicate that the energy dissipation, which correlates with the mixing intensity according to Eq. (6), does not influence the pH and solids mass in co-precipitation in the range investigated. Accordingly, the role of mixing in co-precipitation in the preparation of catalysts is, therefore, disputed.

After co-precipitation is completed, the co-precipitate is aged at conditions where minerals containing both Cu and Zn are formed by recrystallization: preferably zincian malachite for Cu-rich catalysts or additionally aurichalcite ($(Zn,Cu)_5[(CO_3)_2(OH)_6]$) for catalysts with > 28 mol % Zn [25, 26]. A recent study by Güldenpfennig et al. [27] showed that the Zn content also influences phase transformation kinetics. Zincian malachite tends to form needles prone to agglomeration, which define the later catalyst structure on the mesoscale [17]. Promoters such as Al_2O_3 or ZrO_2 with a mass fraction of usually < 15 wt % [28, 29] and up to 44 wt % [30] are precipitated simultaneously to achieve a

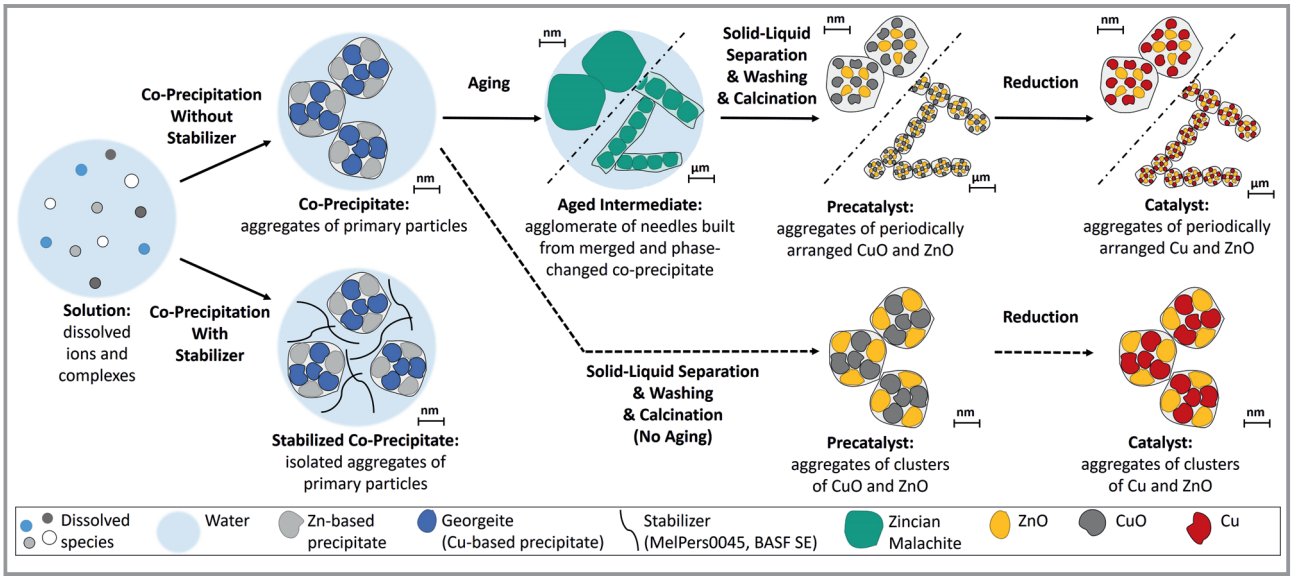

Figure 1. Evolution of microstructure and composition of the catalyst precursors during the multistep preparation of Cu/Zn-based catalysts. Aged intermediate, precatalyst and catalyst are shown at two different size scales.

high homogeneity, but generally do not influence the evolution of Cu/Zn phases during aging [31]. Therefore, we studied a simplified Cu/Zn-based binary catalyst precursor (Sect. 3.1 and 3.2) with no promoters to be considered (Fig. 1).

Catalysts are manufactured in industry by semi-batch co-precipitation in a stirred tank reactor [32], where the co-precipitation and aging overlap in time and space. This overlap happens because the supply of reactants requires several minutes and aging usually takes another 30 min to several hours, while the co-precipitation is completed in milliseconds to seconds [22, 33]. Thus, freshly precipitated particles and particles that have already aged for up to 20 to 60 min [17, 29, 31], coexist with this procedure. A locally limited supply of reactant solutions and the inhomogeneous mixing conditions in the stirred tank reactor may also contribute to the spatial inhomogeneity of the co-precipitation and aging parameters. This makes it rather difficult, if not impossible, to completely control the homogeneity of the co-precipitate and the reproducibility of its preparation [31, 34].

After solid-liquid separation and before calcination, the aged intermediate is washed and dried to remove any residual salts and water, which may reduce the catalytic activity in the MeOH synthesis [18]. If aging were skipped, much larger clusters of pure CuO and ZnO would be formed during calcination (Fig. 1), resulting in a bad catalyst performance [35]. After calcination, the precatalyst is shaped into the macroscopic form desired and reduced in a H_2 atmosphere to obtain the final catalyst material. Influences of the co-precipitation and, to some extent, the aging on catalyst properties are often summarized under the term "chemical memory" [8, 9, 21].

Given the particular importance of this class of catalysts and motivated by the need to quantify fundamental interrelationships, we aim to evaluate how process conditions during the co-precipitation and aging may influence physicochemical properties of the precursors and, subsequently, the catalyst performance. Consequently, the co-precipitation and aging are considered and performed strictly separate of each other using an experimental procedure that could be transferable to production scale. Our approach is to distinguish between hydrochemistry, mixing and solids formation in order to identify individual functional dependencies often summarized as the chemical memory of the catalyst. The focus in this contribution will be on the mixing and the understanding of how it may affect the co-precipitate and, thus, the resulting catalyst structure on the microscale. Optimization of the catalyst composition regarding the DME synthesis from CO_2 is not intended at this time, which is why the reactant composition will not be varied.

2 Materials and Methods

2.1 Materials

We distinguish the following intermediates a to e according to Fig. 1: the co-precipitate (a) consists of individual aggregates composed of pure-phase primary particles (b). Aging results in an aged intermediate (c) composed of needle-shaped aggregates that tend to form agglomerates in the µm-range. These agglomerated needles decompose by calcination into aggregates composed of CuO, ZnO and, if present, ZrO_2, called the precatalyst (d). A final catalyst (e) is then obtainable by the shaping and reduction of CuO to Cu by H_2.

Three catalyst compositions are considered. A simplified binary catalyst precursor based on Cu and Zn (CZ catalyst) is used for the studies on stabilization, mixing and aging, as shown in Sect. 3.1.1, 3.1.2 and 3.2. A ternary CZZ catalyst is used to evaluate transferability of the results between different Cu/Zn-based catalysts in Sect. 3.1 and for material characterization and performance evaluation in Sect. 3.3. Additionally, a commercial CZA catalyst is used to benchmark the results with CZZ in Sect. 3.3.

The reactant solutions were prepared from $Cu(NO_3)_2 \cdot 3H_2O$ (purity ≥ 99 %, Acros Organics), $Zn(NO_3)_2 \cdot 6H_2O$ (purity ≥ 99 %, Alfa Aesar), $ZrO(NO_3)_2 \cdot 6H_2O$ (purity > 99.5 %, Acros Organics), $NaHCO_3$ (purity ≥ 99 %, Carl Roth) and demineralized water. All hygroscopic salts with a tendency to deliquesce were stored inside desiccators to prevent the absorption of water. MelPers 0045 (polycarboxylat ether in water, BASF SE) was used as a stabilizer. H-FER 20 (ferrierte-type zeolite, Zeolyst International) was used as a dehydration catalyst for the DME synthesis. Information on the CZA catalyst can be found elsewhere [29].

2.2 Experimental Setup for Co-Precipitation and Aging

Firstly, continuous co-precipitation and batch aging were strictly separated according to Fig. 2a. This setup was used to investigate the stabilization of the co-precipitate and the influence of mixing on the co-precipitate in Sect. 3.1 and for the aging studies in Sect. 3.2. Furthermore, a continuously co-precipitated catalyst for the precatalyst characterization and performance tests in Sect. 3.3 was prepared with this configuration.

A $NaHCO_3$ solution (feed 1) and a metal nitrate solution (feed 2) with equal volume flows were continuously mixed by an impinging micro jet mixer. Co-precipitation then takes place. The dimensions of the mixer are given in Fig. 2a in mm. The feed solutions for the experiments in Sect. 3.1 and 3.3 were supplied using syringe pumps, as described elsewhere [36]. Two gear pumps (MCP-Z Standard, Ismatec with GJ-N23 pump heads, Micropump) in combination with

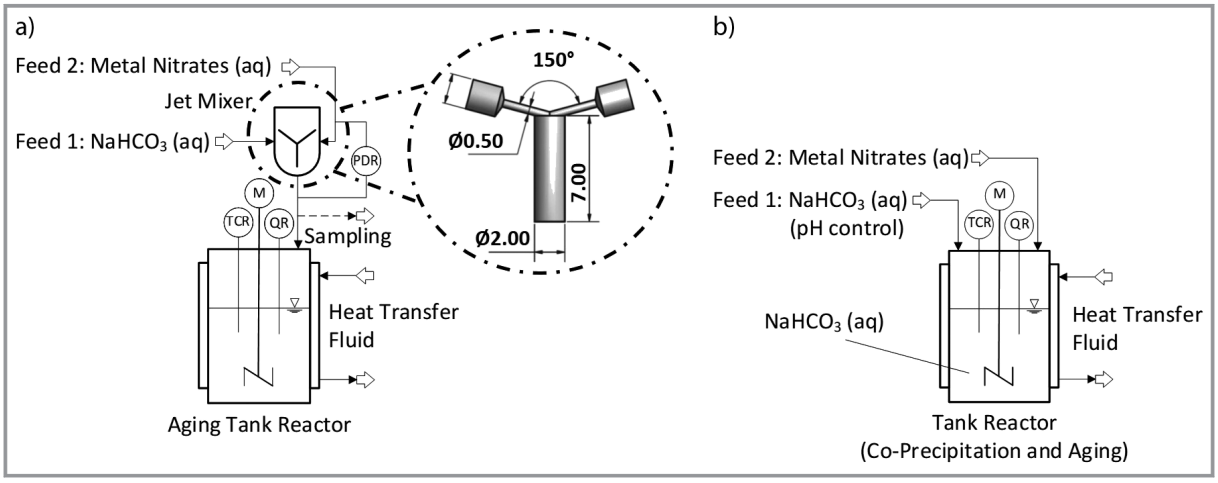

Figure 2. Experimental setups for a continuous co-precipitation followed by batch aging (a) and a semi-batch co-precipitation and aging (b). M: motor, TCR: temperature control and recording, QR: pH recording, PDR: differential pressure recording.

magnetic-inductive flow meters (IFC90, Krohne) were used for the experiments in Sect. 3.2. The current gear pump setup allows total volume flows of up to 800 mL min^{-1} and parallel aging in two 4000-mL reactors. Our co-precipitations of only a few minutes and a solids content of about 5 wt % in the suspension result in a production capacity of more than 200 g aged and dried intermediate per day. The capacity is mostly limited by time-consuming washing of the aged intermediate. A further scale-up of the co-precipitation and aging is possible by either numbering-up or adjusting the micro jet mixer size according to Rehage et al. [37, 38]. Regarding all experiments on the binary catalyst precursor in Sect. 3.1 and 3.2,

$b_{NaHCO_3,Feed1} = 1.01$ mol $kg_{H_2O}^{-1}$,

$b_{Cu(NO_3)_2,Feed2} = 0.18$ mol $kg_{H_2O}^{-1}$,

$b_{Zn(NO_3)_2,Feed2} = 0.09$ mol $kg_{H_2O}^{-1}$ and T = 50 °C were used. Regarding all experiments on the ternary catalyst precursor in Sect. 3.1 and Fig. 3,

$b_{NaHCO_3,Feed1} = 0.38$ mol $kg_{H_2O}^{-1}$,

$b_{Cu(NO_3)_2,Feed2} = 0.06$ mol $kg_{H_2O}^{-1}$,

$b_{Zn(NO_3)_2,Feed2} = 0.03$ mol $kg_{H_2O}^{-1}$,

$b_{Zr(NO_3)_2,Feed2} = 0.01$ mol $kg_{H_2O}^{-1}$ and T = 30 °C were used. The continuously prepared catalyst investigated in Sect. 3.3 was created from solutions with

$b_{NaHCO_3,Feed1} = 1.01$ mol $kg_{H_2O}^{-1}$,

$b_{Cu(NO_3)_2,Feed2} = 0.16$ mol $kg_{H_2O}^{-1}$,

$b_{Zn(NO_3)_2,Feed2} = 0.08$ mol $kg_{H_2O}^{-1}$,

$b_{Zr(NO_3)_2,Feed2} = 0.03$ mol $kg_{H_2O}^{-1}$ at 40 °C resulting in pH = 6.9 after co-precipitation. There were no issues of plugging for these molalities.

The co-precipitate suspension was fed directly into a double-jacketed 4000-mL glass tank reactor (d_{tank} = 120 mm) with four baffles according to DIN 28131, where aging took place under stirring with a three-blade propeller agitator ($d_{stirrer}$ = 50 mm, 30° pitch) at 950 rpm for the aging studies in Sect. 3.2. The pH was measured and temperature controlled with ±1 K accuracy. The further processing into a catalyst for Sect. 3.3 was similar to the procedure for the semi-batch catalyst described below and is specified elsewhere [29]. Samples during aging were obtained by withdrawing suspension near the stirrer. These samples were processed identically to the co-precipitate suspension, as described in Sect. 2.3.

Secondly, a reference material for the precatalyst characterization and catalyst performance tests in Sect. 3.3 following a standard preparation routine is prepared by a conventional semi-batch process, as shown in Fig. 2b, where co-precipitation and aging overlap in time and space [6, 39]. An amount of 1000 mL of 0.2 mol L^{-1} $NaHCO_3$ solution were placed in a 2000-mL reactor. Following the procedure suggested by Arena et al. [6] and Frusteri et al. [39], the reactor was placed inside an ultrasonic bath (Sonorex RK 510 H, Bandelin) at 40 °C and equipped with a two-blade anchor impeller operating at 520 rpm. Then, 100 mL of a 0.8 mol L^{-1} metal nitrate solution with $n_{Cu(NO_3)_2}/n_{Zn(NO_3)_2}/n_{ZrO(NO_3)_2}$ = 6/3/1(feed 2) was transferred into the reactor at a flow rate of 1.6 mL min^{-1}. The pH was maintained between 7.0 and 7.2 by constantly adding a 1 mol L^{-1} $NaHCO_3$ solution (feed 1) dropwise. After feed 2 had been completely fed, the suspension was aged for 2 h at the same conditions without pH adjustment. The suspension was then sedimented using a centrifuge and the solid residue was washed by resuspension in water until no more nitrate could be detected (< 10 mg L^{-1}, MQuant 110020, Merck). Afterwards, the aged intermediate was dried and calcined. All further process details are specified by Polierer et al. [29].

2.3 Analytics

Particle size distributions (PSDs) of samples obtained in Sect. 3.1 were measured by means of dynamic light

scattering (DLS) with a Zetasizer Nano ZS (Malvern Panalytical). Accordingly, a sample of 5 mL of the co-precipitate suspension was directly fed as a free jet into a 1000-mL beaker (d_{beaker} = 95 mm) (about 10 cm travel distance) with a magnetic stirring bar ($d_{stirrer}$ = 40 mm) operating at 300 rpm, baffles and 500 mL of demineralized water. A refractive index of 1.813, a mean value for malachite [40], and an absorption index of 0.3 [41] were used for the solids. The liquid phase was considered as pure water because of the high dilution. Each sample was measured three times to ensure no secondary processes occur that may influence the particle size.

The PSD and morphology were validated by transmission electron microscopy (TEM) with a FEI Osiris ChemiStem (200 kV). Energy-dispersive X-ray spectroscopy (EDXS) using an equipped Bruker Quantax system (XFlash detector) was used to examine the spatially resolved elemental distribution of metals inside the particles and the quantitative metal composition given in Tab. 1. The dried sample was suspended in water by means of an ultrasound bath and then spread on a TEM gold grid using an ultrasonic fogger for both measurements.

Fourier-transform infrared spectroscopy (FT-IR) and X-ray diffraction (XRD) measurements of the dried and ground samples were used to determine the phase composition of the solids in Sect. 3.1 and 3.2. The FT-IR spectra in the range of 4000 $cm^{-1} < \tilde{\nu} < 230\ cm^{-1}$ with a resolution of 2 cm^{-1} were measured using a Varian 660-IR spectrometer (Agilent) in combination with the software Resolution Pro and the KBr disc technique [29]. X-ray diractograms in the range of $5° < 2\theta < 80°$ were measured using a Panalytical X'Pert Pro X-ray diffractometer (Malvern Panalytical) with Bragg-Brentano geometry and Cu K-α radiation with a Ni filter over a period of 120 min.

The co-precipitate suspension was collected without dilution for the TEM, TEM-EDXS, XRD and FT-IR measurements described above. It was then filtered (MN85/70, Macherey-Nagel) using a water aspirator. The filter cake was suspended and washed with demineralized water until an electrical conductivity of < 50 $\mu S\,cm^{-1}$ was achieved and no nitrate could be detected by nitrate test strips (< 10 mg L^{-1}, VWR Chemicals). The moist sample was then dried at $p \geq 1 \cdot 10^{-4}$ mbar and 25 °C for 16 h (Vacutherm VT6130 M-BL, Heraeus with Trivac D16B/DS, Leybold).

The specific copper surface area (S_{Cu}) was determined (subsequent to an H_2 temperature-programmed reduction measurement) by N_2O reactive frontal chromatography using an Advance Optima 2020 continuous gas analyzer (ABB Asea Brown Boveri) [29]. The specific particle surface area (S_{BET}) was determined by N_2 physisorption measurements using a Quantachrome NOVA 2000e device (Anton Paar) at 77 K. Samples were degassed for 12 h at 120 °C. Isotherms were evaluated with the Brunnauer-Emmett-Teller model (BET) in the range of 0.01–0.5 p/p_0.

Catalyst performance was tested in the direct DME synthesis from syngas using a mixture of CZZ, respectively CZA catalysts, for MeOH synthesis and H-FER 20 for DME synthesis from MeOH in a mass ratio of 1:1. The catalysts were then mixed with SiC (Mineraliengroßhandel Hausen GmbH) (mass ratio 1:5) to prevent hotspot formation. Testing was performed in a continuous-flow fixed bed reactor with 12 g of mixed material. The feed gas composition was varied while maintaining a modified gas hourly velocity value of $\dot{V}_{in} = 36\,000\ mL_N g^{-1}_{MeOH\ cat} h^{-1}$ to ensure that conversion took place in the kinetic region. Chromatography, thermal conductivity, flame ionization detection and FT-IR spectroscopy were used for the analysis. More details on catalyst conditioning and testing can be found elsewhere [29, 42].

3 Results and Discussion

The following results and discussion section is structured in accordance with our approach to consider co-precipitation and aging separately in order to characterize and understand the correlations between process conditions and physicochemical properties of the respective intermediates. This knowledge will then be transferred to catalyst preparation to characterize the influence on the final catalyst properties. The significance of our approach for adapting catalyst preparation to changing requirement, e.g., the use of CO_2 for MeOH synthesis, will be evaluated by comparing differently prepared Cu/Zn-based catalysts in combination with a fixed acid dehydration component in direct DME synthesis.

As discussed in Sect. 1, it is known that decomposition during calcination determines the nanostructure of the final catalyst [17], often also referred to as the microstructure [18, 43]. Morphology development during aging determines the mesostructure [17], and shaping can modify the macroscopic structure. In addition, we postulate that the morphology of the co-precipitate influences the structuring of the final catalyst at microscale in a similar manner as that illustrated in Fig. 1. Furthermore, we propose the hypothesis that this very same co-precipitate morphology is a function of co-precipitation kinetics and is, therefore, influenced by mixing, which is to be investigated in Sect. 3.1. Based on these results, the impact on the physicochemical properties of the resulting catalyst is then studied in Sect. 3.3. In addition to the assumptions made regarding the morphology, we assume that the phase composition of the co-precipitate is similarly important since it influences recrystallization kinetics during aging or even the phase composition of the aged intermediate according to a recent study [21]. Therefore, the influence of mixing on the phase composition of the co-precipitate is correspondingly considered in Sect. 3.1.

As time scales of the co-precipitation and aging are significantly different, as described in Sect. 1, we further assume that the former is kinetically limited whereas the latter approaches thermodynamic equilibrium. Therefore, aging is

considered separately in Sect. 3.2. Firstly, a thermodynamic model is used to evaluate whether the phase composition of the aged intermediate can be predicted in terms of a thermodynamic equilibrium state. Secondly, it is determined whether there are options suitable to reach the final state of aging faster, which would be a general advantage for technical processing. Accordingly, the influence of the morphology and composition of the co-precipitate on aging kinetics is examined in Sect 3.2.

Finally, the impact of the newly gained process knowledge and the adapted process design on the catalyst will be evaluated in Sect. 3.3. Consequently, the physicochemical properties and the performance of two differently prepared CZZ catalysts, one by a standard semi-batch approach and one by the adapted process, are compared with those of a commercial CZA catalyst regarding DME productivity.

3.1 Importance of Mixing in Co-Precipitation

As described above, we suggest that the morphology and phase composition of the co-precipitate may be of critical importance as they potentially influence aging kinetics and the microstructure of the final catalyst, which will be discussed in Sect. 3.2 and 3.3. Therefore, it is essential to understand how the co-precipitate is formed and how its physicochemical properties can be controlled.

The driving force for solids formation by precipitation is generally the phase-specific supersaturation S, which is generated when both reactant solutions are mixed. A hypothetical S_{max}, according to Eq. (5), is described solely by hydrochemical models in terms of the activities of solids-forming ions a_i, the solubility product $K_{SP}(T)$ of the solid phase, and the stoichiometric coefficients ν_i and $\nu_\pm$. However, the effective local supersaturation S_{eff} depends on how fast both solutions are mixed on the molecular level and the ensuing local concentrations, respectively, activities a_i of the solids-forming ions i.

$$S = \left(\frac{\prod a_i^{\nu_i}}{K_{SP}(T)} \right)^{1/\nu_\pm} \tag{5}$$

There are at least two different solid phases precipitating simultaneously in co-precipitation. The different phases form common aggregates in the co-precipitation of the Cu/Zn-based catalyst precursor, as is shown schematically in Fig. 1 and as will be shown later in Fig. 3. Our goal is to describe the PSD and phase composition of these aggregates, which are defined as the co-precipitate according to Fig. 1 and Sect. 2.1, based on the hydrochemistry and solids formation kinetics in the future. Therefore, knowledge about the influence of mixing on the resulting co-precipitate properties is essential in order to either additionally model the mixing influence or exclude mixing influences as completely as possible by means of an adapted experimental design.

This chapter is, thus, devoted to the study of the influence of mixing on co-precipitate morphology and composition, see Sect. 3.1.2. Firstly, though, since the co-precipitate has a high tendency for agglomeration, as illustrated in Fig. 1, a method to stabilize the aggregates is discussed in Sect. 3.1.1.

3.1.1 Stabilization of Co-Precipitate for Morphology Studies

It is demonstrated in Sect. 3.1.2 that the morphology and phase composition of the co-precipitate can be controlled by adjusting the process conditions. Firstly, however, it must be clarified why we have defined the co-precipitate, as discussed in Fig. 1 and Sect. 2.1, and how the PSD, as a measurable value for the morphology of this co-precipitate, can be determined.

The TEM-EDXS images of a Cu/Zn/Zr-based co-precipitate at two different sample areas are shown in Fig. 3 to illustrate the metal distribution inside the solids. Based on the total volume flow and the distance between the jet mixer and collecting vessel, about 0.5 s have passed between the first contact of reactants and the dilution of the co-precipitate suspension in water. It is evident that each individual particle is composed of Cu and Zn. However, the clear spatial separation of Cu and Zn atoms indicates that they are not bound in a common crystal lattice but are present as independent phases, which precipitated separately from each other and then formed a common aggregate. The XRD measurements of Cu/Zn-based co-precipitates in Fig. 10, which will be discussed later on, confirm that no zincian malachite or aurichalcite is present. As the amount of Zr in the reactants is low, only a few of the aggregates at the bottom left in Fig. 3b show negligible quantities of Zr. For this reason and due to the independence between Cu/Zn-based phases and promoter phases described in Sect. 1, Zr can be neglected for now. Thus, our definition and simplified representation of the co-precipitate in Fig. 1 are justified and

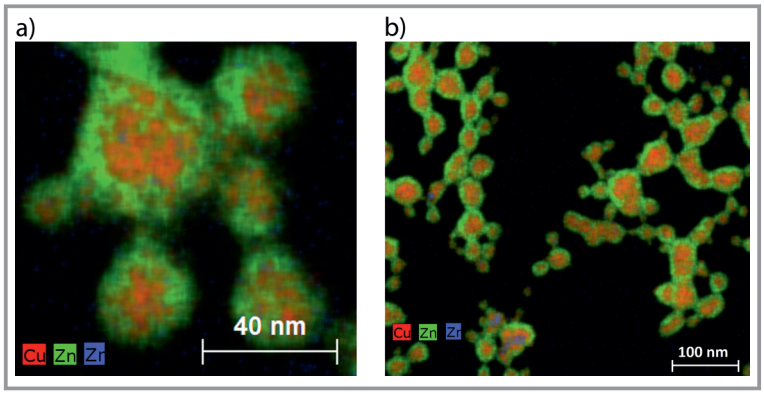

Figure 3. TEM-EDXS images of Cu/Zn/Zr-based co-precipitate for $\dot{V}_{total}$ = 50 mL min^{-1} without stabilizer showing two different sample areas (a) and (b). All metals present are highlighted: Cu in red, Zn in green and Zr in blue.

the binary Cu/Zn-based catalyst precursor is primarily used for mixing studies.

An investigation of the respective Cu- and Zn-based primary particles as a further intermediate in solids formation may be possible using a Cryo-TEM setup, as has been used by Judat and Kind [44] but would go beyond the scope of this work, which is geared towards application. Therefore, we focus on the aggregates as the result of co-precipitation.

It is evident from Fig. 3 that the aggregates tend to agglomerate strongly, as can also be seen in Fig. 4a. A simplified Cu/Zn-based co-precipitate is shown here, again after a process time of about 0.5 s based on the volume flow and experimental setup. The individual aggregates are present in the form of a net-like structure built from the intergrown spherical aggregates. A kinetic description of co-precipitation in terms of nucleation and crystal growth alone and feasible measurement of particle sizes by means of DLS is not possible this way. However, agglomeration of the aggregates can successfully be prevented by adding an electro-steric stabilizer (MelPers0045, BASF SE) to feed 1, as shown in Fig. 4b and schematically depicted in Fig. 1. Here, the individual aggregates are clearly separated from each other and stabilized as spherical particles, which is a prerequisite for DLS measurements. This may also slow down aging processes by preventing particle collisions. In Fig. 4c the volumetric density distribution q_3 measured by means of DLS is plotted as a function of the particle size x when adding the stabilizer to feed 1.

The mean values from three samples, each measured three times in a row, are shown. Small deviations indicate good reproducibility and sufficient suppression of secondary processes during measurement, such as agglomeration and subsequent aging. A volume-based median particle size $\bar{x}_{50,3}$ = 51 ± 3 nm can be calculated according to Eqs. (S1) to (S3) in the Supporting Information (SI). Evaluation of over 1000 particles in TEM images with $c_{\mathrm{MelPers0045,Feed1}}$ = 20 g L^{-1} results in $\bar{x}_{50,3}$ = 53 nm. Thus, DLS in combination with MelPers0045 as a stabilizer is suitable for characterizing the aggregates that we have defined as the co-precipitate.

3.1.2 Physicochemical Properties of Co-Precipitate

The morphology and phase composition of the co-precipitate are, as described in Sect. 3.1, a function of hydrochemistry, solids formation kinetics and mixing influences and, in turn, possibly influence aging and the microstructure of the catalyst. An independent analysis of these correlations shall identify individual functional correlations previously summarized as the chemical memory and will serve for an improved catalyst preparation in Sect. 3.3. Experiments here are based on the condition that all process parameters, apart from mixing intensity, were kept constant to determine the influence of mixing. Continuous co-precipitation in a jet mixer also prevents undefined spatial and temporal fluctuations, e.g., in temperature, pH and reactant concentrations. The co-precipitate morphology is analyzed in terms of the PSD, specific surface area S_{BET} and shape of the aggregates.

Mixing in micro jet mixers is generally limited by the micromixing time τ_{micro} [45] and can, therefore, be described using τ_{micro}. Regarding the turbulent regime, Eq. (6) can be used to calculate $\tau_{\mathrm{micro,turb}}$ as a function of kinematic viscosity ν and the mean energy dissipation $\bar{\varepsilon}$ according to the engulfment model [46, 47]. According to Eq. (7), $\bar{\varepsilon}$ depends on the pressure drop induced by mixing Δp_{Mix}, the density ρ of the mixed fluid, the volume of the mixing zone V_{Mix}, the total volume flow $\dot{V}_{\mathrm{total}} = \dot{V}_{\mathrm{Feed1}} + \dot{V}_{\mathrm{Feed2}}$ and the mass flows $\dot{m}_i$ and mean velocities $\bar{u}_i$ of the feeds and in the outlet, which are all a function of $\dot{V}_{\mathrm{total}}$ [48]. A comparison between different setups limited by micromixing would be possible by calculating $\bar{\varepsilon}$. Here, the same setup for co-precipitation is used for all investigations in Sect. 3.1 and 3.2. Therefore, $\dot{V}_{\mathrm{total}}$ as a directly adjustable parameter is used in this study to display and discuss the results instead.

$$\tau_{\mathrm{micro,turb}} = \frac{12}{\ln(2)} \left(\frac{\nu}{\bar{\varepsilon}}\right)^{0.5} \tag{6}$$

$$\bar{\varepsilon} = \frac{\Delta p_{\mathrm{Mix}} \dot{V}_{\mathrm{total}} + \left(0.5 \dot{m}_{\mathrm{Feed1}} \bar{u}^2_{\mathrm{Feed1}} + 0.5 \dot{m}_{\mathrm{Feed2}} \bar{u}^2_{\mathrm{Feed2}} - 0.5 \dot{m}_{\mathrm{Mix}} \bar{u}^2_{\mathrm{Mix}}\right)}{\rho V_{\mathrm{Mix}}} \tag{7}$$

The volume-based median aggregate size $x_{50,3}$ in Fig. 5 is plotted as a function of the total volume flow $\dot{V}_{\mathrm{total}}$. Two re-

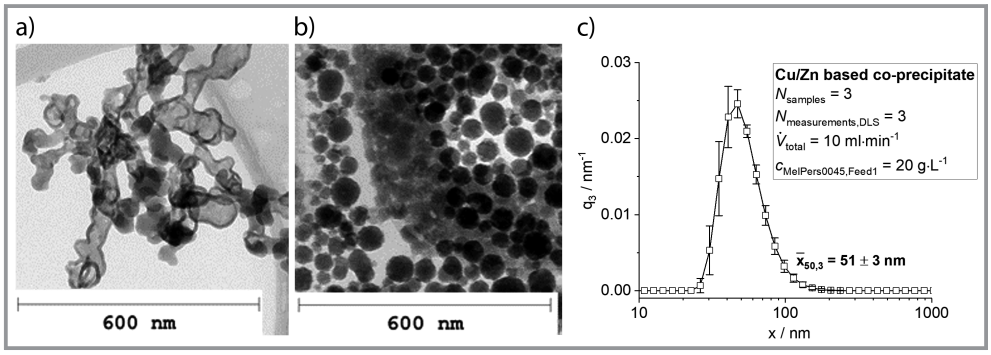

Figure 4. TEM images of Cu/Zn-based co-precipitate for $\dot{V}_{\mathrm{total}}$ = 10 mL min^{-1}. Comparison of the co-precipitation without stabilizer (a) and with $c_{\mathrm{MelPers0045,Feed1}}$ = 20 g L^{-1} (b). c) shows stable and reproducible DLS measurements after successful stabilization of the aggregates.

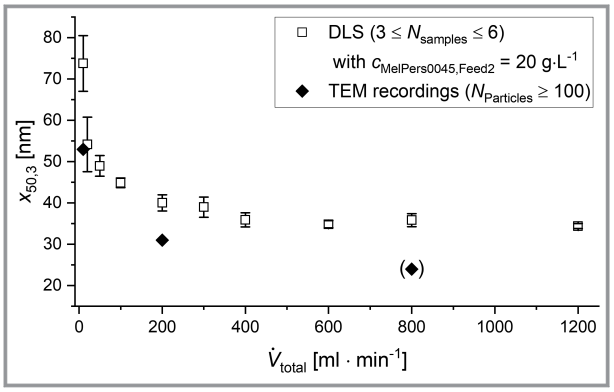

Figure 5. Median particle size $x_{50,3}$ as a function of the total volume flow for a Cu/Zn-based co-precipitate. Comparison of DLS measurements with TEM imaging.

gimes can be distinguished. The particle size decreases for small $\dot{V}_{total}$ with increasing volume flows down to a constant value of $x_{50,3} \approx 35$ nm. Due to lower effective supersaturations, fewer primary particles form, which, in turn, can grow to larger aggregates since the total amount of reactants is constant. For volume flows larger than $\dot{V}_{total} \approx 400$ mL min^{-1}, the particle size is no longer a function of mixing since mixing is faster than solids formation. Furthermore, deviations are much smaller at high volume flows than for $\dot{V}_{total} < 50$ mL min^{-1}. The comparison between TEM and DLS evaluations show larger deviations for higher volume flows. However, $x_{50,3}$ also decreases with larger $\dot{V}_{total}$ when looking exclusively at TEM results. The TEM results for 800 mL min^{-1} have to be interpreted critically due to poor sample quality (cf. Fig. S4 in the SI). Regardless of $\dot{V}_{total}$, each TEM image shows spherical co-precipitate, partly with a strong tendency towards agglomeration (see Fig. S1 to S4).

The specific surface area of the co-precipitate S_{BET} is plotted as a function of $\dot{V}_{total}$ in Fig. 6. Here, similar to Fig. 5, a major increase in surface area for a small $\dot{V}_{total}$ is apparent, while S_{BET} is practically constant for $\dot{V}_{total} \geq 400$ mL min^{-1}, which is to be expected for valid size measurements of increasingly small particles.

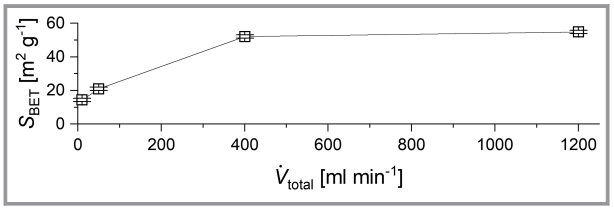

Figure 6. Mass-specific surface area of the Cu/Zn-based co-precipitate as a function of total volume flow.

The influence of $\dot{V}_{total}$ on the solids phase composition of the co-precipitate analyzed by FT-IR spectroscopy is shown in Fig. 7. The complete spectra are shown in Fig. S6. No differences between the positions and relative intensities of bands are apparent for $\dot{V}_{total} = 1200$ mL min^{-1} and $\dot{V}_{total} = 400$ mL min^{-1}, which indicates an identical phase composition. Variations in absolute transmissions may result from different sample sizes. The band in area A corresponds to the phase georgeite expected [17, 19]. A flattening of this band is evident particularly for $\dot{V}_{total} = 10$ mL min^{-1}. Instead, a band in area B emerges for $\dot{V}_{total} \leq 50$ mL min^{-1}. According to Stoilova et al. [49] bands in the region of 760–700 cm^{-1} correspond to the asymmetric O-C-O bending mode of CO_3^{2-} ions and their "intensity […] decreases when copper ions are replaced by zinc ions," indicating less incorporated Zn for volume flows too low. The small band in area C is assigned to metal-oxygen interactions, e.g., Cu-O [49], and remains unchanged for all volume flows.

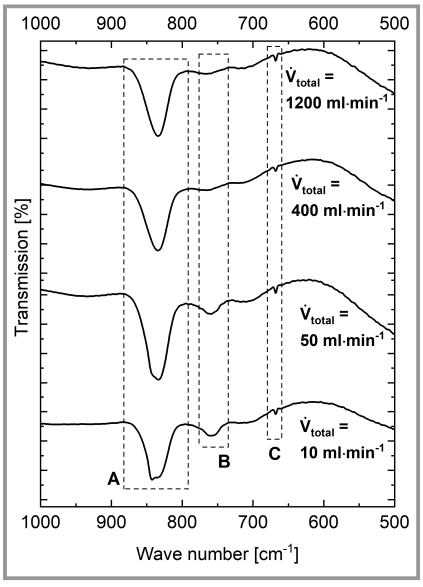

Figure 7. FT-IR spectra for various total volume flows showing the solids phase composition of the Cu/Zn-based co-precipitate. Areas marked with A, B and C correspond to peaks of georgeite [17, 19], asymmetric O-C-O bending mode of CO_3^{2-} ions [49] and metal-O interactions, e.g., Cu-O [49], respectively.

The extent to which the findings are also relevant for ternary catalyst precursors is discussed based on the results shown in Fig. 8. Similar to Fig. 5, the volume-based median aggregate size $x_{50,3}$ is plotted versus $\dot{V}_{total}$, but here for the co-precipitation of a Cu/Zn/Zr-based catalyst precursor. Again, a decrease of $x_{50,3}$ with increasing volume flows is detected until a minimum of $x_{50,3} \approx 25$ nm is reached. However, the median particle size for $\dot{V}_{total} \leq 50$ mL min^{-1} is largely increased compared to the Cu/Zn-based co-precipitate. Deviations and TEM-EDXS evaluations (cf. Fig. S5 in the SI) indicate that the agglomeration at low volume flows is not prevented completely despite adding a stabilizer. A possible explanation is that the Zr species seem to show a different distribution pattern in the solid phase compared to the Cu- and Zn-based precursors. Yet, once a critical mixing time is reached for $\dot{V}_{total} > 400$ mL min^{-1}, mixing

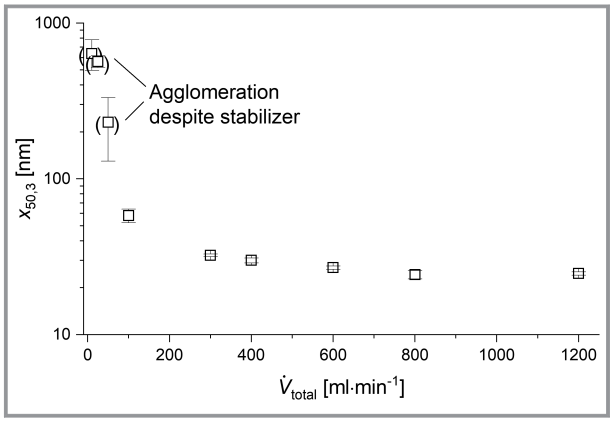

Figure 8. Median particle size $x_{50,3}$ by DLS measurements as a function of the total volume flow for a Cu/Zn/Zr-based co-precipitate.

no longer influences solids formation and agglomeration and significant deviations in aggregate size do not occur.

Our results suggest that two main mixing regimes exist for the co-precipitation of Cu/Zn-based catalyst precursors:

I. Co-precipitation is limited by mixing.
II. Co-precipitation is independent of mixing influences.

In our opinion, this explains the somewhat contradictory statements in the literature (Sect. 1) regarding the influence of mixing in co-precipitation and allows for a unified explanation of the phenomena. A critical volume flow of $\dot{V}_{total,crit} \approx 400\,mL\,min^{-1}$ needs to be chosen for the parameters and experimental setup considered in our work to rule out mixing influences in the co-precipitation and obtain the highest effective supersaturation possible:

$$\lim_{\dot{V}_{total} \to \dot{V}_{total,crit}} S_{eff} = S_{max} \tag{8}$$

If this condition is met, primary particles and, accordingly, the aggregates, decrease in size down to a threshold only limited by solids formation kinetics and, consequently, undefined phase transformation is prevented.

3.2 Role of Aging

Aging is essential to obtain the target phase zincian malachite by recrystallization from the co-precipitate [18]. While co-precipitation is completed within milliseconds to seconds, aging times typically range between 30 min and several hours [22, 33]. Therefore, we postulate that aging is dominated by the drive of the suspension to reach the thermodynamic equilibrium state. Accordingly, we think that the phase composition of the final aged product can be described by an entirely thermodynamic model without considering of kinetics.

A combination of an activity coefficient model and a thermodynamic model were used in the hydrochemistry software PHREEQC [50] to calculate the solids phase composition as a function of pH at 25 °C, as shown in Fig. 9. Details of the models and substance data used are given in Sect. S4 and S5. Reactant concentrations and temperature were chosen according to the experiments on the binary system in Sect. 3.1. The pH was adjusted by adding suitable quantities of HNO_3 or NaOH. Calculations suggest that zincian malachite is the dominant phase for approximately $3 < pH < 12$ with a molar fraction of 0.9 to 1.0 and only small residues of $ZnCO_3 \cdot H_2O$ or aurichalcite. No solids formation is to be expected for $pH < 3$, while CuO becomes prevalent for $pH > 12$. The pH ranges predicted for aurichalcite, CuO and the absence of solids generally agree with titration experiments in which the pH was varied by adding Na_2CO_3 [51]. The dominance of zincian malachite was confirmed experimentally for $5 < pH < 8$ [52]. The influences of $\tilde{c}_{CO_3^{2-}}$ and $\tilde{c}_{OH^-}$ on the phase composition of the aged product can be studied separately from each other in the future by varying the pH independently from the $NaHCO_3$ concentration in the simulation. Elaborate parameter studies could be reduced to a minimum by using such model calculations.

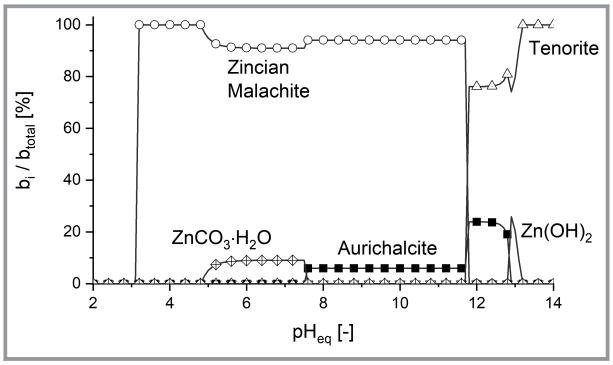

Figure 9. Calculated solids phase composition at thermodynamic equilibrium as a function of pH_{eq}.

For industrial application, the necessary aging time t_{Age} to obtain the requested phase composition is important for economic reasons. Therefore, it was investigated how aging kinetics can be influenced by adjusting the co-precipitation and, thus, the physicochemical properties of the co-precipitate according to Sect. 3.1.2. Accordingly, samples of the Cu/Zn-based catalyst precursor were taken at defined aging times and analyzed by XRD. X-ray diffractograms for four different aging times are plotted for $\dot{V}_{total} = 50\,mL\,min^{-1}$ in Fig. 10a, corresponding to slow mixing during the co-precipitation. In the initial stage, no sharp or intense reflexes are visible, which indicates the presence of an X-ray amorphous co-precipitate as has been repeatedly shown in literature for solids rich in georgeite [18, 24]. After aging for 90 min, the first sharp reflexes are visible, mostly allocated to the known intermediate $Na_2Zn_3(CO_3)_4 \cdot 3H_2O$ and the target phase zincian malachite [22]. The scattering pattern after aging for 300 min is matched to zincian malachite and

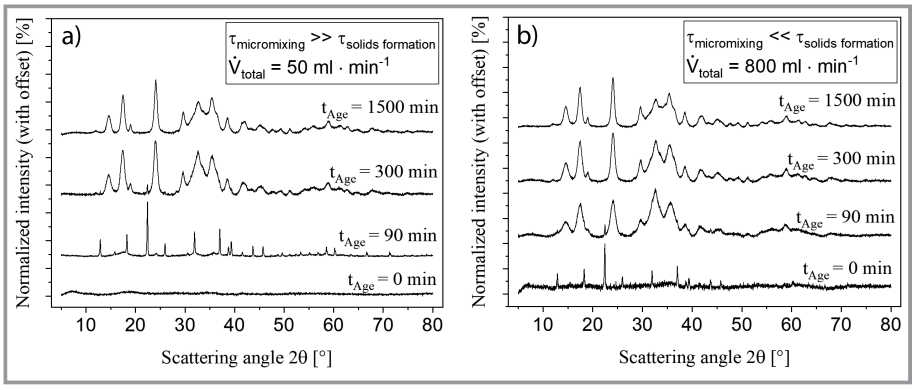

Figure 10. Solids phase composition development during aging by XRD for two samples with slow (a) and fast (b) mixing, respectively, in the preceding co-precipitation.

less than 1 % aurichalcite (see Rietveld refinement calculations in Sect. S3). Further aging no longer changes the crystalline phase composition of the solids.

Corresponding results for $\dot{V}_{total}$ = 800 mL min^{-1}, where mixing no longer influences solids formation according to Sect. 3.1, are shown in Fig. 10b. Here, $Na_2Zn_3(CO_3)_4 \cdot 3H_2O$ is already present directly after co-precipitation. Similarly, the almost identical final crystalline composition of the solids is already observed after 90 min. Thereafter, phase composition does not change notably. We attribute these accelerated aging kinetics to a larger specific surface area of the co-precipitate, in accordance with the findings presented in Fig. 6. The accelerated aging kinetics for fast mixing are also evident in the pH development shown in Fig. S8a and S8b. The distinctive pH drop followed by a steep rise of pH indicating phase transformation occurs after 76 min for fast mixing while it takes 94 min for slow mixing. This is in agreement with the XRD spectra shown in Fig. 10.

The experimentally determined predominance of zincian malachite with small amounts of aurichalcite for $t_{Age} \rightarrow \infty$ is independent of the mixing conditions. After aging for 1500 min, the pH for slow mixing is 8.36 while the pH for fast mixing is 8.81. Thus, the calculations shown in Fig. 9 are in agreement with the experimental results and indicate that aging can be predominantly described in terms of thermodynamic equilibrium. However, in accordance with our initial hypothesis, aging kinetics can be modifiable by tuning the particle morphology of the co-precipitate.

3.3 Effect of Co-Precipitation on Catalyst Properties and Performance

Finally, the potential for catalyst optimization by strictly separating co-precipitation and aging will be discussed. In this context, our hypothesis that the co-precipitate morphology influences the later microstructure of the catalyst is to be discussed.

Accordingly, two CZZ catalysts are compared: one from a standard semi-batch preparation with low volume flows where the co-precipitation and aging overlap in time and space, and one prepared by continuous co-precipitation with $\dot{V}_{total}$ = 300 mL min^{-1} followed by batch aging. Additionally, a commercial CZA catalyst is used as a benchmark. Tab. 1 reveals similar mass fractions of copper for all three precatalysts after calcination [29]. However, the continuously prepared catalyst has approximately twice the mass specific surface and copper surface areas as the precatalyst from the semi-batch preparation. The continuously prepared CZZ catalyst also exceeds S_{BET} and S_{Cu} of the commercial CZA catalyst.

Table 1. Relevant physicochemical properties of the precatalysts considered for performance tests from [29].

Catalyst	x_{Cu} [wt %]	S_{BET} [m^{2}g^{-1}]	S_{Cu} [m^{2}g^{-1}]
Continuous (lab scale)	61	125	27
Semi-batch (lab scale)	57	65	10
Commercial (CZA catalyst)	64	98	13

A comparison of TEM-EDXS images for the two CZZ precatalysts shown in Fig. 11 also indicates differences in the microstructure [29]. Large areas of pure copper and zinc enrichments exist for the semi-batch co-precipitation. By contrast, the continuously prepared catalyst shows a very

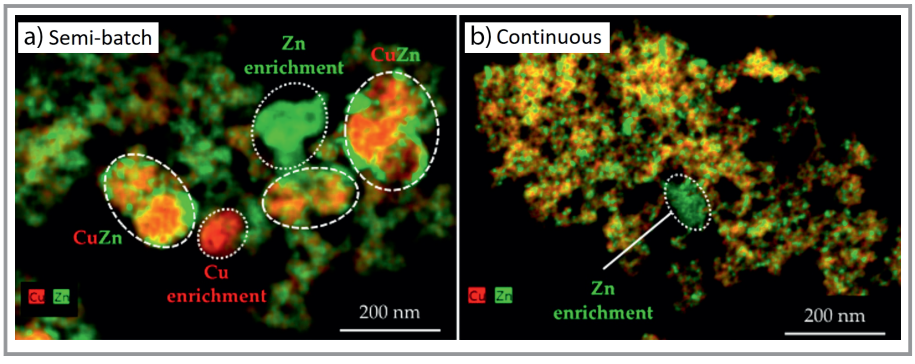

Figure 11. TEM-EDXS images of CuO/ZnO/ZrO_2 precatalysts prepared by semi-batch co-precipitation (a) and continuous co-precipitation at $\dot{V}_{total}$ = 300 mL min^{-1} (b) from [29].

homogeneous and fine distribution of copper and zinc atoms with only a few cluster areas. These differences in metal distribution are again attributed to generally more uniform and smaller primary particles and, consecutively, aggregates after co-precipitation as indicated in Fig. 8. We believe that there is some "morphological memory" throughout aging and calcination, which possibly explains the much higher S_{Cu} of the calcined catalyst. This, furthermore, confirms that co-precipitation, and thus the co-precipitate morphology, affect the microstructure of the later catalyst. Further images that also show the Zr distribution can be found in the literature [29].

All three catalysts were used in direct DME synthesis to evaluate how the differences in physicochemical properties effect catalyst performance. The DME productivity is plotted in Fig. 12 as a function of the volumetric ratio of CO_2 to (CO_2 + CO) in the syngas at a constant H_2 fraction [29]. The continuously prepared CZZ catalyst consistently exhibits a higher productivity than the semi-batch catalyst. The commercial benchmark catalyst shows a constantly better performance than the semi-batch catalyst prepared at lab scale but is inferior to the continuously prepared catalyst. The expectations based on the properties featured in Tab. 1 and Fig. 11 were met accordingly.

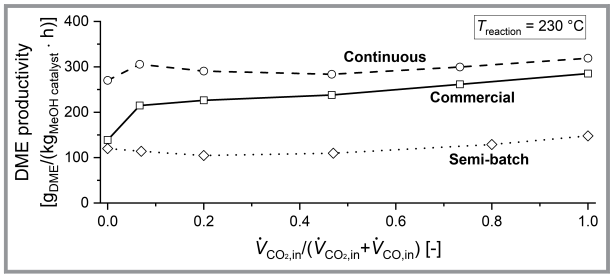

Figure 12. Dimethyl ether (DME) productivity as a function of the volumetric ratio of CO_2 to (CO + CO_2) in the syngas for three different catalysts. Continuous: Cu/ZnO/ZrO_2 catalyst prepared by continuous co-precipitation at lab scale. Semi-batch: Cu/ZnO/ZrO_2 catalyst prepared by semi-batch co-precipitation at lab scale. Commercial: Cu/ZnO/Al_2O_3 catalyst; as purchased. Synthesis parameters: p = 50 bar, $\dot{V}_{in}$ = 36 000 mL $g^{-1}_{MeOH\ cat}$ h^{-1}. Data from [29].

In summary, how co-precipitation is carried out in detail has a significant influence on the subsequent particle properties, i.e., the microstructure of the precatalyst, and, thus, product properties of the final catalyst material. Obviously, one major factor is how mixing during co-precipitation influences the effective supersaturation and, therefore, particle formation and, in turn, the resulting aggregate morphology.

4 Conclusion

In this study, continuous co-precipitation and batch aging to prepare methanol catalyst precursors were strictly separated and investigated with particular emphasis on the subsequent steps of mixing, initial solids formation, and recrystallization. The complex formation of Cu/Zn-based precursors was regarded with enhanced temporal and spatial resolution in order to fundamentally understand the individual processes finally yielding catalysts with improved physicochemical properties and performance.

The role of mixing in continuous co-precipitation was studied detached from hydrochemistry and solids formation kinetics. Agglomeration of co-precipitate and, thus, aging were prevented by using a stabilizer. Two mixing regimes were determined for a Cu/Zn-based precursor. One at low volume flows, which are equivalent to slow micro mixing, where the aggregate size of the co-precipitate decreases with increasing volume flows. The second mixing regime exists at sufficiently high volume flows above $\dot{V}_{total}$ = 400 mL min^{-1}, where a threshold is reached and solids formation is no longer influenced by mixing. Accordingly, S_{BET} of the co-precipitate initially increases and then remains approximately constant. Furthermore, slow mixing results in a slightly altered metal composition in the solid phase. Volume flow studies on the more complex Cu/Zn/Zr-based precursor show that these findings can in general be transferred to similar metal compositions.

We described the phase transformation during aging by a thermodynamic equilibrium model showing that the solids phase composition after aging as a function of the pH is in good agreement with experimental findings. Additionally, it could be shown experimentally that slow mixing during co-precipitation leads to larger particles and, thus, slower aging kinetics than for fast mixing. However, the phase composition for $t_{Age} \rightarrow \infty$ is independent from the mixing conditions and coherent with the thermodynamic calculations.

The influence of the continuous co-precipitation approach for the catalyst performance in direct DME synthesis was investigated for a Cu/ZnO/ZrO_2 catalyst, in comparison to its preparation from semi-batch co-precipitation and to a commercial Cu/ZnO/Al_2O_3 catalyst. Significantly higher DME productivity was achieved with the continuously co-precipitated Cu/ZnO/ZrO_2 catalyst, also independent of the syngas feed composition. The increased activity is in line with larger S_{BET} and S_{Cu} as well as the more homogeneous metal distribution of the latter, which reaffirms our hypothesis that the co-precipitate morphology influences the microstructure of the final catalyst significantly.

Our experimental setup at the moment allows a production capacity of more than 200 g aged and dried precursor per day when operating the micromixer for approx. 20 min in total proving a promising potential for the technical application in catalyst production. Production rates of well over 500 g h^{-1} of aged intermediate should be achievable when operating the micromixer constantly. Further scale-up is possible, either by numbering-up or using the approach of complete similarity.

Our approach to handle initial co-precipitation and subsequent aging strictly separated from each other and to describe the underlying functional dependencies on the

respective intermediates also separately, opens potential for further process optimization. Future work will focus on detailed kinetic modeling of co-precipitation with the goal to understand better and, thus, control the evolution of the morphology and the phase composition of the co-precipitate. Complementarily, the thermodynamic aging model will be extended and validated to temperatures above 25 °C. This will have the potential to predict the influences of co-precipitation and aging parameters on the physicochemical properties of the precursor materials on the basis of these models and to accelerate further catalyst development accordingly.

Supporting Information

Supporting Information for this article can be found under DOI: 10.1002/cite.202100197. This section includes additional references to primary literature relevant for this research [53–72].

The authors thank their students Florian Kreißig, Kassian Armbruster, Sebastian Fernández and Xuelan Zhou and colleagues at IKFT and TVT for their work in the lab and workshop. They kindly acknowledge the Laboratory for Electron Microscopy at Karlsruhe Institute of Technology for TEM(-EDXS) measurements. Further thanks to BASF SE for providing MelPers0045 for our studies. Open access funding enabled and organized by Projekt DEAL.

Symbols used

a	[–]	activity
b	$\left[\text{mol kg}_{\text{H}_2\text{O}}^{-1}\right]$	molality
c	$[\text{g L}^{-1}]$	mass concentration
$\tilde{c}$	$[\text{mol L}^{-1}]$	molar concentration
K_{SP}	[–]	solubility product
$\dot{m}$	$[\text{kg s}^{-1}]$	mass flow
n	[mol]	amount of substance
p	[mbar]	pressure
Δp_{Mix}	[mbar]	pressure drop by mixing
pH	[–]	pH value
S	[–]	supersaturation
S_{BET}	$[\text{m}^2\text{g}^{-1}]$	mass-specific surface area
S_{Cu}	$[\text{m}^2\text{g}^{-1}]$	mass-specific copper surface area
T	[°C]	temperature
t_{Age}	[min]	aging time
$\bar{u}$	$[\text{m s}^{-1}]$	mean velocity
V	$[\text{m}^3]$	volume
$\dot{V}$	$[\text{mL min}^{-1}]$	volume flow
$\dot{V}_{\text{in}}$	$\left[\text{mL g}_{\text{MeOH cat}}^{-1}\text{h}^{-1}\right]$	modified gas-hourly space velocity (GHSV)
x	[nm]	particle size
x_{Cu}	[wt %]	mass fraction of copper in the solids

Greek letters

$\bar{\varepsilon}$	$[\text{W kg}^{-1}]$	mean energy dissipation
ν	[–]	stoichiometric coefficient
ν	$[\text{m}^2\text{s}^{-1}]$	kinematic viscosity
$\tilde{\nu}$	$[\text{cm}^{-1}]$	wavenumber
ρ	$[\text{kg m}^{-3}]$	density
θ	[°]	scattering angle
τ	[ms]	time

Sub- and Superscripts

±	all ions of a salt
0	standard conditions
50,3	volume-based median
BET	Brunnauer-Emmett-Teller model
cat	catalyst
crit	critical
eff	effective
eq	at the thermodynamic state of equilibrium
i	solids-forming ion
in	inlet current into the synthesis reactor
max	maximum
Mix	Mixing zone
micro	micromixing
turb	turbulent

Abbreviations

BET	Brunnauer-Emmett-Teller model
CZ	copper/zinc
CZA	copper/zinc/aluminium
CZZ	copper/zinc/zirconium
DLS	dynamic light scattering
DME	dimethyl ether
EDXS	energy-dispersive X-ray spectroscopy
FT-IR	Fourier-transform infrared spectroscopy
H-FER 20	ferrierte-type zeolite
MeOH	methanol
PSD	particle size distribution
TEM	transmission electron microscopy
XRD	X-ray diffraction

References

[1] S. Simon Araya, V. Liso, X. Cui, N. Li, J. Zhu, S. L. Sahlin, S. H. Jensen, M. P. Nielsen, S. K. Kær, *Energies* **2020**, *13 (3)*, 596. DOI: https://doi.org/10.3390/en13030596

[2] E. Brown, T. Edmonds, R. W. Joyner, J. J. McCarroll, S. R. Tennison, *Catal. Lett.* **2014**, *144 (4)*, 545–552. DOI: https://doi.org/10.1007/s10562-014-1226-4
[3] G. A. Olah, *Angew. Chem., Int. Ed.* **2005**, *44 (18)*, 2636–2639. DOI: https://doi.org/10.1002/anie.200462121
[4] M. Bjørgen, F. Joensen, M. Spangsberg Holm, U. Olsbye, K.-P. Lillerud, S. Svelle, *Appl. Catal., A* **2008**, *345 (1)*, 43–50. DOI: https://doi.org/10.1016/j.apcata.2008.04.020
[5] M. Behrens, F. Studt, I. Kasatkin, S. Kühl, M. Hävecker, F. Abild-Pedersen, S. Zander, F. Girgsdies, P. Kurr, B.-L. Kniep, M. Tovar, R. W. Fischer, J. K. Nørskov, R. Schlögl, *Science* **2012**, *336 (6083)*, 893–897. DOI: https://doi.org/10.1126/science.1219831
[6] F. Arena, K. Barbera, G. Italiano, G. Bonura, L. Spadaro, F. Frusteri. *J. Catal.* **2007**, *249 (2)*, 185–194. DOI: https://doi.org/10.1016/j.jcat.2007.04.003
[7] A. Sternberg, A. Bardow. *ACS Sustainable Chem. Eng.* **2016**, *4 (8)*, 4156–4165. DOI: https://doi.org/10.1021/acssuschemeng.6b00644
[8] C. Baltes, S. Vukojevic, F. Schuth, *J. Catal.* **2008**, *258 (2)*, 334–344. DOI: https://doi.org/10.1016/j.jcat.2008.07.004
[9] M. Behrens, R. Schlögl, *Z. Anorg. Allg. Chem.* **2013**, *639 (15)*, 2683–2695. DOI: https://doi.org/10.1002/zaac.201300356
[10] Y. Choi, K. Futagami, T. Fujitani, J. Nakamura, *Appl. Catal., A* **2001**, *208 (1–2)*, 163–167. DOI: https://doi.org/10.1016/S0926-860X(00)00712-2
[11] S. Kuld, M. Thorhauge, H. Falsig, C. F. Elkjær, S. Helveg, I. Chorkendorff, J. Sehested, *Science* **2016**, *352 (6288)*, 969–974. DOI: https://doi.org/10.1126/science.aaf0718
[12] T. Fujitani, J. Nakamura, *Appl. Catal., A* **2000**, *191*, 111–129. DOI: https://doi.org/10.1016/S0926-860X(99)00313-0
[13] M. Kurtz, H. Wilmer, T. Genger, O. Hinrichsen, M. Muhler, *Catal. Lett.* **2003**, *86 (1/3)*, 77–80. DOI: https://doi.org/10.1023/A:1022663125977
[14] N. Mota, R. Guil-Lopez, B. G. Pawelec, J. L. G. Fierro, R. M. Navarro, *RSC Adv.* **2018**, *8 (37)*, 20619–20629. DOI: https://doi.org/10.1039/C8RA03291B
[15] F. Arena, G. Italiano, K. Barbera, S. Bordiga, G. Bonura, L. Spadaro, F. Frusteri. *Appl. Catal., A* **2008**, *350 (1)*, 16–23. DOI: https://doi.org/10.1016/j.apcata.2008.07.028
[16] L. Zwiener, F. Girgsdies, D. Brennecke, D. Teschner, A. G. Machoke, R. Schlögl, E. Frei, *Appl. Catal., B* **2019**, *249*, 218–226. DOI: https://doi.org/10.1016/j.apcatb.2019.02.023
[17] M. Behrens, *J. Catal.* **2009**, *267 (1)*, 24–29. DOI: https://doi.org/10.1016/j.jcat.2009.07.009
[18] B. Bems, M. Schur, A. Dassenoy, H. Junkes, D. Herein, R. Schlögl, *Chem. – Eur. J.* **2003**, *9 (9)*, 2039–2052. DOI: https://doi.org/10.1002/chem.200204122
[19] A. M. Pollard, M. S. Spencer, R. G. Thomas, P. A. Williams, J. Holt, J. R. Jennings, *Appl. Catal., A* **1992**, *85 (1)*, 1–11. DOI: https://doi.org/10.1016/0926-860X(92)80125-V
[20] X. Jiang, L. Zheng, Z. Wang, J. Lu, *J. Mol. Catal. A: Chem.* **2016**, *423*, 457–462. DOI: https://doi.org/10.1016/j.molcata.2016.07.046
[21] X. Jiang, X. Qin, C. Ling, Z. Wang, J. Lu, *AIChE J.* **2018**, *124 (2-3)*, 123. DOI: https://doi.org/10.1002/aic.16168
[22] Q.-C. Zhang, K.-P. Cheng, L.-X. Wen, K. Guo, J.-F. Chen, *RSC Adv.* **2016**, *6 (40)*, 33611–33621. DOI: https://doi.org/10.1039/C6RA02512A
[23] G. Simson, E. Prasetyo, S. Reiner, O. Hinrichsen, *Appl. Catal., A* **2013**, *450*, 1–12. DOI: https://doi.org/10.1016/j.apcata.2012.06.040
[24] M. A. Hartig, N. Jacobsen, W. Peukert, *Chem. Eng. Sci.* **2014**, *109*, 158–170. DOI: https://doi.org/10.1016/j.ces.2014.01.026
[25] A. Tarasov, J. Schumann, F. Girgsdies, N. Thomas, M. Behrens, *Thermochim. Acta* **2014**, *591*, 1–9. DOI: https://doi.org/10.1016/j.tca.2014.04.025
[26] M. Behrens, F. Girgsdies, A. Trunschke, R. Schlögl, *Eur. J. Inorg. Chem.* **2009**, *2009 (10)*, 1347–1357. DOI: https://doi.org/10.1002/ejic.200801216
[27] A. Güldenpfennig, M. Distaso, W. Peukert, *Chem. Eng. J. (Amsterdam, Neth.)* **2019**, *369*, 996–1004. DOI: https://doi.org/10.1016/j.cej.2019.03.088
[28] M. Kulawska, M. Madej-Lachowska, *Chem. Process Eng.* **2013**, *34 (4)*, 479–496. DOI: https://doi.org/10.2478/cpe-2013-0039
[29] S. Polierer, D. Guse, S. Wild, K. Herrera Delgado, T. N. Otto, T. A. Zevaco, M. Kind, J. Sauer, F. Studt, S. Pitter, *Catalysts* **2020**, *10 (8)*, 816. DOI: https://doi.org/10.3390/catal10080816
[30] F. Arena, G. Italiano, K. Barbera, G. Bonura, L. Spadaro, F. Frusteri, *Catal. Today* **2009**, *143 (1-2)*, 80–85. DOI: https://doi.org/10.1016/j.cattod.2008.11.022
[31] J. Schumann, T. Lunkenbein, A. Tarasov, N. Thomas, R. Schlögl, M. Behrens, *ChemCatChem* **2014**, *6 (10)*, 2889–2897. DOI: https://doi.org/10.1002/cctc.201402278
[32] A. Wolf, V. Michele, O. F.-K. Schlüter, F. Herbstritt, J. Heck, L. Mleczko, *Chem. Eng. Technol.* **2015**, *38 (11)*, 2017–2024. DOI: https://doi.org/10.1002/ceat.201500040
[33] S. Kaluza, M. Behrens, N. Schiefenhövel, B. Kniep, R. Fischer, R. Schlögl, M. Muhler. *ChemCatChem* **2011**, *3 (1)*, 189–199. DOI: https://doi.org/10.1002/cctc.201000329
[34] M. Behrens, *Catal. Today* **2015**, *246*, 46–54. DOI: https://doi.org/10.1016/j.cattod.2014.07.050
[35] D. M. Whittle, A. A. Mirzaei, J. S. J. Hargreaves, R. W. Joyner, C. J. Kiely, S. H. Taylor, G. J. Hutchings, *Phys. Chem. Chem. Phys.* **2002**, *4 (23)*, 5915–5920. DOI: https://doi.org/10.1039/b207691h
[36] R. T. Kügler, M. Kind, *Chem. Eng. Process.* **2016**, *101*, 25–32. DOI: https://doi.org/10.1016/j.cep.2015.12.007
[37] H. Rehage, M. Bartsch, M. Kind, *Chem. Eng. J.* **2020**, 125763. DOI: https://doi.org/10.1016/j.cej.2020.125763
[38] H. Rehage, M. Kind, *Chem. Eng. Sci.* **2021**, *229*, 116007. DOI: https://doi.org/10.1016/j.ces.2020.116007
[39] F. Frusteri, M. Cordaro, C. Cannilla, G. Bonura, *Appl. Catal., B* **2015**, *162*, 57–65. DOI: https://doi.org/10.1016/j.apcatb.2014.06.035
[40] J. D'Ans, E. Lax, *Elemente, anorganische Verbindungen und Materialien, Minerale*, 4th ed., Taschenbuch für Chemiker und Physiker, Band III, Springer, Berlin **1998**.
[41] www.malvernpanalytical.com/en/learn/knowledge-center/technical-notes/TN101104SelectingParticleAbsorbtionLaserDiffractio (Accessed on October 18, 2021)
[42] S. Wild, S. Polierer, T. A. Zevaco, D. Guse, M. Kind, S. Pitter, K. Herrera Delgado, J. Sauer, *RSC Adv.* **2021**, *11 (5)*, 2556–2564. DOI: https://doi.org/10.1039/D0RA09754C
[43] M. Behrens, S. Zander, P. Kurr, N. Jacobsen, J. Senker, G. Koch, T. Ressler, R. W. Fischer, R. Schlögl, *J. Am. Chem. Soc.* **2013**, *135 (16)*, 6061–6068. DOI: https://doi.org/10.1021/ja310456f
[44] B. Judat, M. Kind, *J. Colloid Interface Sci.* **2004**, *269 (2)*, 341–353. DOI: https://doi.org/10.1016/j.jcis.2003.07.047
[45] B. K. Johnson, R. K. Prud'homme, *AIChE J.* **2003**, *49 (9)*, 2264–2282. DOI: https://doi.org/10.1002/aic.690490905
[46] L. Metzger, M. Kind, *Chem. Eng. Res. Des.* **2016**, *109*, 464–476. DOI: https://doi.org/10.1016/j.cherd.2016.02.019
[47] J. Baldyga, J. R. Bourne, *Chem. Eng. J.* **1989**, *42 (2)*, 83–92. DOI: https://doi.org/10.1016/0300-9467(89)85002-6
[48] S. W. Siddiqui, Y. Zhao, A. Kukukova, S. M. Kresta, *Ind. Eng. Chem. Res.* **2009**, *48 (17)*, 7945–7958. DOI: https://doi.org/10.1021/ie801562y
[49] D. Stoilova, V. Koleva, V. Vassileva, *Spectrochim. Acta, Part A* **2002**, *58 (9)*, 2051–2059. DOI: https://doi.org/10.1016/S1386-1425(01)00677-1

[50] www.usgs.gov/software/phreeqc-version-3 (Accessed on October 20, 2021)
[51] M. Behrens, D. Brennecke, F. Girgsdies, S. Kißner, A. Trunschke, N. Nasrudin, S. Zakaria, N. F. Idris, S. B. A. Hamid, B. Kniep, R. Fischer, W. Busser, M. Muhler, R. Schlögl, *Appl. Catal., A* **2011**, *392 (1-2)*, 93–102. DOI: https://doi.org/10.1016/j.apcata.2010.10.031
[52] S. Zander, B. Seidlhofer, M. Behrens, *Dalton Trans.* **2012**, *41 (43)*, 13413–13422. DOI: https://doi.org/10.1039/c2dt31236k
[53] T. J. Collins, *BioTechniques* **2007**, *43 (1 Suppl)*, 25–30. DOI: https://doi.org/10.2144/000112517
[54] N. Doebelin, R. Kleeberg, *J. Appl. Crystallogr.* **2015**, *48 (Pt 5)*, 1573–1580. DOI: https://doi.org/10.1107/S1600576715014685
[55] M. Behrens, F. Girgsdies, *Z. Anorg. Allg. Chem.* **2010**, *636 (6)*, 919–927. DOI: https://doi.org/10.1002/zaac.201000028
[56] D. L. Parkhurst, C. A. J. Appelo, *User's guide to PHREEQC (Version 2): A computer program for speciation, batch-reaction, one-dimensional transport, and inverse geochemical calculations*, U.S. Geological Survey, Denver, CO **1999**. DOI: https://doi.org/10.3133/wri994259
[57] D. L. Parkhurst, C. A. J. Appelo, *Description of Input and Examples for PHREEQC Version 3–A Computer Program for Speciation, Batch-Reaction, One-Dimensional Transport, and Inverse Geochemical Calculations*, U.S. Geological Survey, Denver, CO **2013**. http://pubs.usgs.gov/tm/06/a43 (Accessed on October 23, 2021)
[58] A. K. Alwan, J. H. Thomas, P. A. Williams, *Transition Met. Chem.* **1980**, *5 (1)*, 3–5. DOI: https://doi.org/10.1007/BF01396855
[59] M. Haderlein, A. Güldenpfennig, D. Segets, W. Peukert, *Comput. Chem. Eng.* **2017**, *98*, 197–208. DOI: https://doi.org/10.1016/j.compchemeng.2016.12.007
[60] S. Hagemann, T. Scharge, T. Willms, *Entwicklung einer thermodynamischen Datenbasis für ausgewählte Schwermetalle, Gesellschaft für Anlagen- und Reaktorsicherheit*, Köln **2015**. DOI: https://www.doi.org/10.13140/RG.2.1.3121.0082
[61] C. E. Harvie, N. Møller, J. H. Weare, *Geochim. Cosmochim. Acta* **1984**, *48 (4)*, 723–751. DOI: https://doi.org/10.1016/0016-7037(84)90098-X
[62] H. T. Kim, W. J. Frederick, *J. Chem. Eng. Data* **1988**, *33 (2)*, 177–184. DOI: https://doi.org/10.1021/je00052a035
[63] I. A. Kiseleva, L. P. Ogorodova, L. V. Melchakova, M. R. Bisengalieva, N. S. Becturganov, *Phys Chem Minerals* **1992**, *19 (5)*. DOI: https://doi.org/10.1007/BF00204009
[64] www.nist.gov/srd/nist46 (Accessed on October 23, 2021)
[65] K. S. Pitzer, *J. Phys. Chem.* **1973**, *77 (2)*, 268–277. DOI: https://doi.org/10.1021/j100621a026
[66] K. S. Pitzer, G. Mayorga, *J. Phys. Chem.* **1973**, *77 (19)*, 2300–2308. DOI: https://doi.org/10.1021/j100638a009
[67] K. S. Pitzer, G. Mayorga, *J. Solution Chem.* **1974**, *3 (7)*, 539–546. DOI: https://doi.org/10.1007/BF00648138
[68] K. J. Powell, P. L. Brown, R. H. Byrne, T. Gajda, G. Hefter, S. Sjöberg, H. Wanner, *Pure Appl. Chem.* **2007**, *79 (5)*, 895–950. DOI: https://doi.org/10.1351/pac200779050895
[69] R. A. Reichle, K. G. McCurdy, L. G. Hepler, *Can. J. Chem.* **1975**, *53 (24)*, 3841–3845. DOI: https://doi.org/10.1139/v75-556
[70] J. M. Santana-Casiano, M. González-Dávila, F. J. Millero, *J. Solution Chem.* **2008**, *37 (6)*, 749–762. DOI: https://doi.org/10.1007/s10953-008-9274-2
[71] P. Taylor, *Solubility and Stability of Inorganic Carbonates: An Approach to the Selection of a Waste Form for Carbon 14*, Whiteshell Nuclear Research Establishment, Pinawa, Manitoba **1987**. https://inis.iaea.org/collection/NCLCollectionStore/_Public/20/062/20062977.pdf (Accessed on October 23, 2021)
[72] D. Turner, M. Whitfield, A. Dickson, *Geochim. Cosmochim. Acta* **1981**, *45 (6)*, 855–881. DOI: https://doi.org/10.1016/0016-7037(81)90115-0

DOI: 10.1002/cite.202100197

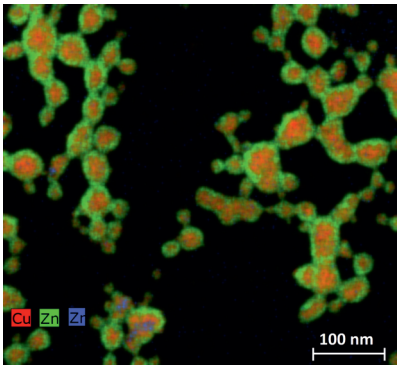

Improved Preparation of Cu/Zn-Based Catalysts by Well-Defined Conditions of Co-Precipitation and Aging

David Guse, Sabrina Polierer, Stefan Wild, Stephan Pitter, Matthias Kind**

Research Article: Two mixing regimes in the continuous co-precipitation are revealed using a modified method to prepare Cu/Zn-based catalysts. Furthermore, the influence of mixing on aging kinetics, the microstructure development of the catalyst and the catalyst performance is investigated to evaluate the usefulness of our approach for adapting catalyst preparation to new demands on the material, possibly also at an industrial scale. .....

Supporting Information available online

